Title

Multiple Core and Vibronic Coupling Effects in Attosecond Stimulated X-Ray Raman Spectroscopy (SXRS).

Permalink

Journal

Authors

Hua, Weijie
Biggs, Jason
Zhang, Yu
et al.

Publication Date

DOI

Multiple Core and Vibronic Coupling Effects in Attosecond Stimulated X-Ray Raman Spectroscopy (SXRS)

Weijie Hua, **Jason D. Biggs**, **Yu Zhang**, **Daniel Healion**, **Hao Ren**, and **Shaul Mukamel**[*]
Department of Chemistry, University of California, Irvine, CA 92697-2025, United States

Abstract

Attosecond Stimulated X-ray Raman Spectroscopy (SXRS) is a promising technique for investigating molecular electronic structure and photochemical processes with high spatial and temporal resolution. We present a theoretical study of SXRS from multiple core excitation sites of the same element. Two issues are addressed: interference between pathways contributing the signals from different sites; and how nuclear vibrations influence the signals. Taking furan as a model system, which contains two types of carbons C_α and C_β, we performed time-dependent density functional theory calculations and computed the SXRS signals with two pulses tuned at the carbon K-edge. Our simulations demonstrate that the SXRS signal from the C_α and C_β sites are non-additive, owing to the significant mixed contributions (C_α 1s excitations by the pump pulse followed by C_β 1s excitations by the probe, or vice verse). Harmonic vibrations linearly coupled to the electronic transitions are incorporated using the cumulant expansion. The nuclei act as a bath for electronic transitions which accelerate the decay of time-domain signal. The frequency-domain spectrum is modified by a small red shift and high-resolution fine-structure features are introduced.

1 Introduction

The time-domain attosecond stimulated X-ray Raman spectroscopy (SXRS) technique[1–6] is often considered as an extension of the frequency-domain resonant inelastic X-ray scattering (RIXS) spectroscopy,[7,8] which offers higher flexibility in controlling parameters. In SXRS measurements with two well-separated pulses,[9] the pulse carrier frequencies are tuned for core-excitations of the same or different elements. After the interaction with each impulsive pulse, the created core hole rapidly decays and the system goes back to a superposition of the ground and valence-excited states. The intermediate core-excited states provide selectivity to the populated valence excited states and the signals. Experimental implementation requires bright light and ultrashort light sources, such as the X-ray free electron laser.[10] All-X-ray stimulated Raman measurements are gradually coming up.[11] Extensive theoretical progress has been made during the past decade.[1–6] Various computational methods of signals have been suggested based on the equivalent core hole (ECH),[12–14] static exchange (STEX),[15,16] and time-dependent density function theory (TDDFT)[17,18] methods.

Our early stimulated Raman works covered several core edges including N1s, O1s, and S2p, in molecules where only one core hole is created. One goal of this article is to address carbon K-edge signal which is more complex owing to multiple sites of the same element. Fundamental questions must be addressed, such as symmetry, the localized or delocalized nature of the core hole, and whether or not the signals are additive. Contributions of

---

[*]To whom correspondence should be addressed smukamel@uci.edu.

different cores to X-ray absorption near edge structure [XANES, *i.e.*, near-edge X-ray fine-structure (NEXAFS) or X-ray absorption (XAS)] spectra are additive but nonlinear signals are expected to be nonadditive due to pathways involving lots of different carbon atoms, the valence orbitals are different for different core states. A second issue we address is nuclear dynamics, or more specifically vibronic coupling. All applications so far assumed vertical excitations and deexcitations at the ground-state geometry. Nuclear dynamics must be included for signals involving time delays > 10 fs which exceed the vibrational periods. Taking the vibronic coupling into account is essential to reproduce the vibrational fine structure in high-resolution X-ray spectra. This has been well illustrated in X-ray photoemission (XPS), XANES, and RIXS spectra.[7,19–22]

We choose furan (C_4H_4O, Figure 2a) as our model system with two types of carbons sites and vibronic coupling. Vibrationally-resolved calculations for SXRS signals will be performed. Energies, spectroscopies, and nuclear dynamics of this system have been widely studied, and is conceptually used in benchmark demonstration of new theoretical methods or performance comparison of different theoretical levels (refs 23–41 and references therein). In this C_{2V}-symmetry molecule, the four carbons are categorized into two types C_α and C_β, whose 1s electrons differ by ca. 1 eV in energy. With such a small chemical shift, both C_α 1s and C_β 1s electrons can be excited by one pulse, since an attosecond pulse bandwidth covers several to a few tens of eVs in the energy region. Nonlinear spectroscopy under these conditions resembles homonuclear NMR signals. This leads to four channels in the C1sC1s SXRS spectroscopy, denoted as αα, ββ, αβ, and βα. The additivity of the spectrum can be examined by comparing the direct addition of pure signals (αα + ββ) with the total signal (αα + ββ + αβ + βα). The furan molecule has shown evidence of vibronic coupling effect in XPS spectrum.[19,28]

This article is organized as follows: In Section 2, we derive general equations for the vibrationally-resolved SXRS signal after a brief review of the electronic-only formulae. Computational details on the C1sC1s SXRS spectrum are given in Section 3. We then analyze the additivity of the spectrum, study the dependence in pulse width and carrier frequency, and examine the effect of vibronic coupling. Concluding remarks are given in Section 5.

2 Theory

2.1 Stimulated X-ray Raman spectroscopy

In the experiment described here, the system interacts with two resonant X-ray pulses with delay τ. The electric field at position $\boldsymbol{r}$ and time t is

$$\boldsymbol{E}(\boldsymbol{r},t;\tau)=\boldsymbol{e}_2\mathscr{E}_2(t-\tau)e^{i\boldsymbol{k}_2\cdot\boldsymbol{r}-i\omega_2(t-\tau)}+\boldsymbol{e}_1\mathscr{E}_1(t)e^{i\boldsymbol{k}_1\cdot\boldsymbol{r}-i\omega_1 t}+\text{c.c.} \quad (1)$$

Here $\boldsymbol{e}_j$, $\boldsymbol{k}_j$, ω_j, and $\mathscr{E}_j$ represent the electric polarization vector, wave vector, central carrier frequency, and temporal envelope, respectively, and c.c. stands for complex conjugate. We assume a Gaussian envelope

$$\mathscr{E}_j(t)=A_j\exp\left[-\frac{(t-t_0)^2}{2\sigma_j^2}\right] \quad (2)$$

for both the pump and probe pulses (j = 1, 2, respectively). σ_j is the pulse duration, and A_j is the complex amplitude. The pulse spectral envelope is given by

$$\tilde{\mathscr{E}}_j(\omega) = \int_{-\infty}^{+\infty} dt \mathscr{E}_j(t) e^{i\omega t} = A_j \sqrt{2\pi} \sigma_j \exp(i\omega t_0) \exp\left(-\frac{\sigma_j^2 \omega^2}{2}\right). \quad (3)$$

The SXRS experimental setup and loop diagrams are shown in Figure 1. We follow the our previous notations.[3–6,42] g denotes the electronic ground state, g' and g'' are the valence-excited states, and e and e' are the core-excited states. Each pulse j interacts twice with the molecule. This is described by the effective polarizability operator σ_j[3–5]

$$\hat{\sigma}_j = \sum_{g'g''} \sigma_{j;g'g''} |g'\rangle\langle g''|, \quad (4)$$

$$\alpha_{j;g'g''} = \sum_e (e_j \cdot V_{g'e})(e_j \bullet V_{eg''}) O_{j;eg'g''}, \quad (5)$$

$$O_{j;eg'g''} \equiv A_j^2(-i\pi\sigma_j^2)\exp\left(-\frac{\sigma_j^2}{2}[(\Delta_{j;eg'})^2 + (\Delta_{j;eg''})^2]\right) \times \mathrm{erfc}\left(-i\sigma_j \frac{\Delta_{j;eg'} + \Delta_{j;eg''}}{2}\right). \quad (6)$$

In the above expressions, $V_{g'e} = \langle g'|\hat{\mu}|e\rangle$ denotes the transition dipole moment between states g' and e with $\hat{\mu} = \sum_{l=1}^{N} \hat{r}_l$ the electric dipole operator, $\Delta_{j;eg'} = \omega_j - \omega_{eg'} + i\Gamma_e$ is the detuning with $\omega_{eg'}$ the vertical excitation frequency and Γ_e the (half width at half maximum, HWHM) core hole life-time broadening. $\mathrm{erfc}(z) = 1 - \frac{2}{\sqrt{\pi}} \int_0^z du e^{-u^2}$ is the complementary error function. In the interaction picture, $\hat{\alpha}_j$ becomes

$$\hat{\alpha}_j(\tau) = \sum_{g'g''} \alpha_{j;g'g''} \exp(i\omega_{g'g''}\tau - \Gamma_{g'g''}\tau)|g'\rangle\langle g''|. \quad (7)$$

The SXRS signal is given by,[3–5]

$$\mathbb{S}(\tau) = -2\mathrm{Im}\langle g|\hat{\alpha}_2''(\tau)\hat{\alpha}_1(0)|g\rangle. \quad (8)$$

Here $\hat{\alpha}_2'' = (\hat{\alpha}_2 - \hat{\alpha}_2^\dagger)/(2i)$ denotes the anti-Hermitian component of $\hat{\alpha}_2$, which combines the contributions of the two loop diagrams (Figure 1). The signal can be recast in the form

$$\mathbb{S}(\tau) = i\sum_{g'}[\alpha_{2;gg'}''\alpha_{1;g'g}\exp(-i\omega_{g'g}\tau - \Gamma_{gg'}\tau) - \alpha_{2;gg'}''\alpha_{1;g'g}^*\exp(i\omega_{g'g}\tau - \Gamma_{gg'}\tau)]. \quad (9)$$

Fourier transform with respect to τ leads to the frequency-domain signal

$$\mathbb{S}(\Omega) = \sum_{g'}\left[\frac{\alpha_{2;gg'}''\alpha_{1;g'g}}{\omega_{g'g} - \Omega - i\Gamma_{gg'}} + \frac{\alpha_{2;gg'}''\alpha_{1;g'g}^*}{\omega_{g'g} + \Omega + i\Gamma_{gg'}}\right]. \quad (10)$$

Here the two terms correspond respectively to the two terms in eq 9. Since the same information is carried in the positive- and negative-Ω region,[6] we only display the positive-Ω region

$$\mathbb{S}(\Omega)=-\sum_{g'}\frac{\alpha''_{2;gg'}\alpha_{1;g'g}}{\Omega-\omega_{g'g}+i\Gamma_{gg'}};\Omega>0 \quad (11)$$

2.2 Vibrationally-resolved SXRS signals

Owing to the short duration (attoseconds) of the X-ray pulses, nuclear motions can be neglected during the pulses, but take place during the delay period τ. The total adiabatic Hamiltonian in the valence excitation space can be written as,

$$\hat{H}=|g\rangle\hat{H}_g\langle g|+\sum_{g'}|g'\rangle H_{g'}\langle g'|, \quad (12)$$

where $\hat{H}_g$ ($\hat{H}_{g'}$) is the nuclear Hamiltonian of the ground (valence-excited) state, taken to be harmonic.[43–46]

$$\hat{H}_g=\frac{1}{2}\sum_k^M\left[-\hbar^2\frac{\partial^2}{\partial Q_k^2}+\varpi_k^2 Q_k^2\right], \quad (13)$$

$$\hat{H}_{g'}=\frac{1}{2}\sum_k^M\left[-\hbar^2\frac{\partial^2}{\partial Q_k^2}+\varpi_k^2(Q_k+d_{k,g'})^2\right]+\hbar\omega_{gg'}^0. \quad (14)$$

Here ϖ_k is the frequency of vibrational mode k (M is the number of modes) and Q_k stand for the normal coordinates of the ground state. We assume the same curvature of potential energy surface of valence excited state g' and ground state g, while they differ by a displacement $d_{k,g'}$ along the normal coordinates. This linear coupling model (LCM) is commonly used to simulate various linear and nonlinear spectroscopic signals (see, e.g., refs 20,47,48). We adopt this model here for simplicity since it allows to include many electronic states at a low computational cost. Including quadratic coupling and Duschinsky rotation[49] will be a natural future extension. The bare electronic transition energy $\omega_{g'g}^0$ in eq 13 is related to the vertical electronic transition energy $\omega_{g'g}$ in eq 11,

$$\hbar\omega_{g'g}=\hbar\omega_{g'g}^0+\frac{1}{2}\sum_k^M\varpi_k^2 d_{k,g'}^2, \quad (15)$$

where the second term is the vibrational reorganization energy. (In this work the electronic transition energies are evaluated at the ground-state equilibrium geometry, and $\omega_{g'g}$ is obtained directly from the electronic structure simulations.)

The ground electronic state wavefunction can be factorized as,

$$|g,\boldsymbol{n}\rangle=|g\rangle|\boldsymbol{n}\rangle, \quad (16)$$

where $|\boldsymbol{n}\rangle=\prod_k^M|n_k\rangle$ is the nuclear wavefunction, given by a product of contributions from individual modes. Since the nuclear coordinates are frozen during the interaction with the attosecond pulse, the effective polarizability $\hat{\alpha_j}$ is taken to be a purely electronic operator which is diagonal in the nuclear subspace.

The SXRS signal (eq 8) now becomes,

$$\mathbb{S}(\tau) = -2\mathrm{Im}\langle g, \boldsymbol{n}|\exp(\frac{i}{\hbar}\hat{H}\tau)\hat{\alpha}_2''\exp(-\frac{i}{\hbar}\hat{H}\tau)\hat{\alpha}_1|g, \boldsymbol{n}\rangle. \quad (17)$$

This can be recast as

$$\mathbb{S}(\tau) = -2\mathrm{Im}\sum_{g'}\hat{\alpha}_{2;gg'}''\hat{\alpha}_{1;g'g}J_{g'}(\tau), \quad (18)$$

where

$$J_{g'}(\tau) \equiv \langle \boldsymbol{n}|\exp(\frac{i}{\hbar}H_g\tau)\exp(-\frac{i}{\hbar}H_{g'}\tau)|\boldsymbol{n}\rangle. \quad (19)$$

is the linear response function for the vibronic subspace consisting of electronic states g and g', with the transition dipoles set to unity. Applying the second order cumulant expansion[50] to eq 19 yields

$$J(\tau) = \exp[-i\omega_{g'g}\tau - g_{g'}(\tau) - \Gamma_{gg'}\tau], \quad (20)$$

$$g_{g'}(\tau) \equiv \sum_k^M S_{k,g'}[\coth(\frac{\hbar\varpi_k}{2k_\mathrm{B}T})(1 - \cos(\varpi_k\tau)) + i(\sin(\varpi_k\tau) - \varpi_k\tau)], \quad (21)$$

$$S_{k,g'} = \frac{\varpi_k d_{k,g'}^2}{2\hbar}. \quad (22)$$

Here $g_{g'}(\tau)$ is the line broadening function of the valence-excited state g', $S_{k,g'}$ is the Huang-Rhys factor, k_B and T denote the Boltzmann constant and temperature, respectively. The frequency-domain signal is obtained by a numerical Fourier transform of eq 18,

$$\mathbb{S}(\Omega) = \int_0^\infty \mathbb{S}(\tau)e^{i\Omega\tau}. \quad (23)$$

The above expressions assume a fixed orientation between the pulse polarization and the molecule, as indicated by the dot product in eq 6. A statistical average over orientations is required to describe randomly oriented samples.[5] This is summarized in the Appendix.

3 Computational Details

3.1 Excited states

Geometries and vibrational frequencies were computed at the density functional theory (DFT) level with the B3LYP functional[51] and the cc-pVTZ basis set[52] by using the GAMESS-US 2010 program.[53] At the optimized geometry, singlet valence and C1s core excited states are computed with the time-dependent DFT (TDDFT) method in conjunction with the Tamm-Dancoff approximation [TDA, i.e, the configuration interaction singlets (CIS) approximation][54] by using the NWChem package.[55] The same functional is employed and the aug-cc-pVTZ basis set[52] is used for better description of Rydberg states. At this level, the valence and core excited sates can be expressed as:

$$|g'\rangle=\sum_{uv}C_v^u\hat{a}_u^\dagger\hat{a}_v|g\rangle, \quad (24)$$

$$|e\rangle=\sum_{uc}C_c^u\hat{a}_u^\dagger\hat{a}_c|g\rangle. \quad (25)$$

Here $\hat{a}^\dagger$ and $\hat{a}$ represent the creation and annihilation operators of the Kohn-Sham orbitals. Indexes c, v, u loop over the C1s core, valence, and unoccupied MOs, respectively. C_v^u or C_c^u stands for the CI expansion coefficients. With the CI coefficients and molecular orbitals (MOs), the transition dipole matrices between $|g'\rangle$ and $|e\rangle$ can be computed via the Slater-Condon rule,[4,56]

$$\langle g'|\hat{\mu}|e\rangle=\sum_{uvc}\langle v|\hat{\boldsymbol{r}}_1|c\rangle(C_v^u)^*C_c^u. \quad (26)$$

For core excited state and X-ray absorption spectroscopy calculations, we used the restricted excitation window (REW) TDDFT approach.[18] Other implementations by TDDFT are given in refs 17,57–62.

Furan has 4 symmetry-adapted canonical (spatial) MOs that correspond to the C1s electrons: $1b_2$, $2a_1$, $2b_2$, and $3a_1$ (see Figure 2a for a graphical view). They are known as C_α 1s ($1b_2$ and $2a_1$) and C_β 1s ($2b_2$ and $3a_1$) orbitals.[63] The former are 1.3 eV lower. In addition to core excitations from all C1s orbitals, we also performed calculations where core-excitations were restricted to only the C_α 1s or C_β 1s orbitals. The energy levels are depicted in Figure 2b. These will be used in the subsequent spectroscopy calculations to analyze the additivity of nonlinear signals.

3.2 XANES, UV absorption, and SXRS spectra

We first calculate the C1s XANES spectra. These are used to validate the accuracy of the quantum chemical calculations and to guide the settings of the pulse in the consequent SXRS computations. The orientationally-averaged oscillator strength for transition from $|g\rangle$ to $|e\rangle$ is given by[64]

$$f_{eg}^{\text{tot}}=\frac{2m\omega_{eg}}{3\hbar}\sum_{\hat{o}=\hat{x},\hat{y},\hat{z}}|\langle e|\hat{o}|g\rangle|^2, \quad (27)$$

We have also analyzed the in-plane $1s\rightarrow\pi^*$ and out-of-plane $1s\rightarrow\sigma^*$ excitations. In our calculations, the furan molecule in placed in the yz-plane, the corresponding oscillator strength is thus given by[65]

$$f_{eg}^{\pi^*}=\frac{2m\omega_{eg}}{3\hbar}|\langle e|\hat{x}|g\rangle|^2, \;\; f_{eg}^{\sigma^*}=\frac{2m\omega_{eg}}{3\hbar}\sum_{\hat{o}=\hat{y},\hat{z}}|\langle e|\hat{o}|g\rangle|^2. \quad (28)$$

The XANES intensity is given by sum over oscillator strengths of all pairs of transitions, for instance,

$$I_{eg}^{\text{tot}}(E)=\sum_e f_{eg}^{\text{tot}}\delta(E-\hbar\omega_{eg}). \quad (29)$$

We use a Gaussian line shape with HWHM of 0.2 eV instead of the δ function to broaden the calculated stick spectra. To fit the first resolved peak with experiment,[66] we have shifted the calculated spectra by +10.6 eV.

The UV spectrum similarly is given by

$$I_{g'g}^{\text{tot}}(E) = \sum_{g'} f_{g'g}^{\text{tot}} \delta(E - \hbar\omega_{g'g}), \quad (30)$$

$$f_{g'g}^{\text{tot}} = \frac{2m\omega_{g'g}}{3\hbar} \sum_{\hat{o}=\hat{y},\hat{z}} |\langle g'|\hat{o}|g\rangle|^2. \quad (31)$$

We have also used a Gaussian broadening with HWHM of 0.2 eV.

We calculated the SXRS signal with parallel polarizations of the pump and probe pulses. We choose the carrier frequency ω_j at 285.7 eV, which is the first peak in the calculated XANES spectroscopy, and pulse duration at $\sigma_j = 100$ as (FWHM of power spectrum 10.96 eV). HWHM life-time broadening of $\Gamma_{g'} = 0.05$ eV[6] for the valence-excited states and $\Gamma_e = 0.075$ eV[67] for the C1s core-excited states are used. In the gas phase, the experimental first ionization energy of furan is 8.99 eV,[68] and the C1s ionization potential is 290.33 (C_β) and 291.60 eV (C_α).[28] We only consider the bound states. This gives 28 valence-excited states (up to 8.89 eV) and 62 core-excited states (up to 290.30 eV). We only look at the window up to 8.0 eV for valence excitations (15 states).

3.3 The Huang-Rhys factors

The Huang-Rhys displacements were calculated numerically. For each normal mode k, we perform TDDFT/TDA calculations at five structures slightly displaced along each normal coordinate ($Q_k = 0, \pm\delta_k, \pm2\delta_k$). Then potential energy surface (PES) of excited state g' is fitted to the quadratic form,

$$U_{g'}(Q_k) = a_{k,g'}(Q_k - d_{k,g'})^2 + b_{k,g'}. \quad (32)$$

Since there are 21 modes, TDDFT/TDA calculations for valence excitations have been performed at altogether 85 geometries. Different values of δ_k's ranging from $0.1\text{au} \cdot \sqrt{\text{amu}}$ (for high-frequency modes) to $1.6\text{au} \cdot \sqrt{\text{amu}}$ (for low-frequency modes) are set for different modes, which makes the energy difference of the same excited state at these five points be about a few eVs. This choice balances the numerical accuracy of quantum chemistry calculations (requiring a larger δ_k to see the energy difference) and keeping the harmonic picture (a smaller δ_k). Calculations were performed using the Dynavib package.[69] Other ways for calculating the displacements from numerical or analytical gradients of the excited-state PES are given in, for example, refs 20,22,48,70.

4 Results and Discussion

4.1 XANES spectra

Figure 3 displays the simulated C1s XANES spectra calculated by restricting excitations from C_α 1s, C_β 1s, and all C 1s orbitals (panels a, b, and c, respectively). Three major π absorption peaks are observed at 285.7 (C_α), 286.7 (C_β), and 287.0 (C_α) eV. Several strong σ transitions appear at higher frequencies around 287.6, 288.8, and 289.8 eV. Calculated spectra agree well with experiment[66] with major features reproduced. Major π transitions correspond to core excited states 2, 6, and 7, respectively. These are actually the lowest three $^1B_1$ core excited states, as determined by the dipole selection rules. In panel d, we show the corresponding natural transition orbital (NTO) pairs,[71] which help visualize the transitions. In this picture, each transition is represented by a few hole and particle orbitals (NTO pairs). These can be assigned as C 1s $\rightarrow \pi^*$ (b_1) or C 1s $\rightarrow \pi^*$ (a_2) transitions. Each of

these major transitions is described by 2 pairs of NTOs (with different weights). This is caused by the degeneracy of the symmetry-adapted core MOs (a_1 and b_2). XANES signals (eq 29) are additive, i.e., given by sums over contributions from different core orbitals. This is numerically verified in panel c, where the total spectra (black line) look virtually the same as the direct sum of the corresponding results in panels a and b (gold line). Small deviations are because of some mixing of underlying transitions from C_α 1s and C_β 1s orbitals.

4.2 SXRS spectra

4.2.1 Core excitations and nonadditivie contributions—Figure 4 shows the computed SXRS signals from different core excitation channels, either C_α 1s or C_β 1s, for the interactions with the pump and probe pulses. We denote $\alpha\alpha$ or $\beta\beta$ the pure signals with only C_α 1s or C_β 1s orbitals involved; while $\alpha\beta$ or $\beta\alpha$ represent mixed paths. The SXRS signal is nonadditive from the evident difference between simple addition of pure signals ($\alpha\alpha + \beta\beta$) and the total signal ($\alpha\alpha+\beta\beta+\alpha\beta+\beta\alpha$). This is more clearly shown by the real part of signal (middle panel) where the three major features A, B, and C are labeled. We notice that cancellation of pure and mixing signals at peak B and enhancement at peaks A and C. The mixing-channel contributions have comparable magnitudes to the pure ones.

4.2.2 The dominant valence excitations in SXRS—The absolute SXRS signal is decomposed in Figure 5a. Major peaks A, B, C can be assigned as excitations to the valence excited states 1 (1^1A_2), 6 (2^1A_1), and 13 (3^1A_1) at 5.54, 6.70 and 7.70 eV, respectively. Computed excitation energies compare well with early experiments and other theoretical results (see refs 23,27,34,40,41 and references therein). For instance, the experimental energy of state 1 is 5.54 eV;[23] theoretical excitation energies of state 6 are about 6.19–6.79 eV.[34] The corresponding NTO pairs are given in panel b. States 1 and 13 are Rydberg states. Only 1 dominant NTO pair is involved in each case, corresponds to $\pi \rightarrow$ 3s-Ryd and $\pi \rightarrow$ p-Ryd transitions, respectively. While for state 6, two dominant pairs appear with identical weights (occupation numbers 0.705 and 0.704). These are $\pi \rightarrow \pi^*$ excitations. Note that the dominant states here all have zero or very weak oscillator strengths in the UV absorption spectrum (Figure 6), so one can see that SXRS can probe excited states that are inaccessible by UV spectroscopy. Figure 6 shows the good agreement between the simulated and experimental[24] UV spectra. The UV spectrum is given here to compare with the SXRS signal at the same level. Higher level models will be required to account for the conical intersections and vibronic coupling.[30]

4.2.3 Influence of pulse parameters—Figure 7 depicts the absolute SXRS signals for different pulse durations with $\sigma_j = 100, 200, 400$, and 800 as, with the central carrier frequency still kept at 285.7 eV. The corresponding power spectrum FWHM bandwidth (10.96, 5.48, 2.74, and 1.37 eV) is shown by the gray dashes in Figure 3c. As the pulse bandwidth becomes narrower the signal becomes more selective. For $\sigma_j = 800$ as, all other contributions are filtered out except for the lowest valence transition. The signal magnitude decays rapidly as the pulse duration is increased.

We further examined the SXRS dependence on pulse central carrier frequency. Signals are recorded with the frequency scanned from 280.0 to 288.7 eV by an increment of 0.1 eV, while the pulse width is fixed at 400 as. In Figure 8a, the lowest excited state at 5.54 eV serves as the most accessible state, with extremely strong signals at a carrier frequency of ca. 284–285.5 eV. This is because this energy region facilitates both the upward (from ground to core-excited states) and downward (from core to the first valence excited states) excitations with a balance. Apart from the lowest excited state, the valence excitation at 6.7 eV also exhibits relatively strong signals. The above scanning was repeated for $\sigma_j = 100$ as.

In this case, the frequency-domain pulse amplitude remains almost a constant (Figure 3c), so resulting signal only changes by a uniform scaling but keeps the profile shape.

4.2.4 Vibronic coupling—Signals with and without the vibronic coupling are compared in Figure 9. In the time domain, including the vibronic coupling accelerates the decay of the signal, since the nuclei act as a bath to the electronic transitions. In the frequency domain, the vibronic coupling signal causes a 0.1–0.2 eV red shift while the general profile is unaffected (panels c). The shift corresponds to the reorganization energy (eq 15). The vibrational coupling also introduces fine structure: Peak A is split into a double peak, peak B becomes much broader, and high frequency shoulder appears in peak C. The dominant vibrational modes are analyzed in Table 1 in terms of the vibronic coupling strength (i.e., square root of the Huang-Rhys factor). For each valence excited state, only several out of the totally 21 modes have dominant contributions. As seen in Figure 10, these Frank-Condon active modes are all in-plane, symmetric vibrational modes. They cover a range of 900 to 1500 cm^{-1} and both the ring vibrations and C-H scissoring modes are involved. We found that the vibrationally-resolved spectrum is unaffected by varying the temperature between absolute zero and room temperature. This is because all relevant vibrations have higher frequencies compared to $k_B T$.

5 Conclusions

We have analyzed the C1sC1s attosecond Stimulated X-ray Raman Spectroscopy (SXRS) of furan for multiple excitation sites of the same element. By decomposing the two core excitations in a SXRS experiment into the C_α or C_β channels, we demonstrate that the SXRS signals are nonadditive for different carbon sites. The contribution of the mixing channels (C_α 1s excitations by the pump pulse followed by C_β 1s excitations by the probe, or vice verse) is significant. This study provides insights in understanding the interaction of atoms with similar but different chemical properties. Vibronic coupling has been incorporated using the cumulant expansion. We found that it accelerates the decay of signal in the time domain. Vibrational reorganization energy causes a red shift of the signal, and adds fine structure in the frequency domain. For furan, only several in-plane symmetric vibration modes play an important rule in the vibrationally resolved spectroscopy. The signal nonaddtivity and vibronic coupling effect in SXRS spectroscopy should be common to other multidimensional X-ray techniques.

Acknowledgments

Appendix

Orientationally averaged signals

To consider the statistical effect over random-oriented molecules, an ensemble average should be done over the $(e_j \cdot V_{g'e})(e_j \cdot V_{eg''})$ term in eq 6. The orientationally averaged time-domain SXRS signal is given by,[72]

$$\bar{\mathbb{S}}(\tau) = \begin{pmatrix} \mathbb{S}^I(\tau) \\ \mathbb{S}^{II}(\tau) \\ \mathbb{S}^{III}(\tau) \end{pmatrix}^\mathsf{T} \begin{pmatrix} 4 - 2\cos^2\theta \\ 3\cos^2\theta - 1 \\ 3\cos^2\theta - 1 \end{pmatrix}, \quad (33)$$

where $\cos \theta = \langle e_1 | e_2 \rangle$,

$$\mathbb{S}^{\mathrm{I}}(\tau) = i \sum_{g'} \mathrm{tr}(\alpha''_{2;gg'})\mathrm{tr}(\alpha_{1;g'g})W_{g'}, \quad (34)$$

$$\mathbb{S}^{\mathrm{II}}(\tau) = i \sum_{g'} \mathrm{tr}[(\alpha''_{2;gg'})^{\mathsf{T}}(\alpha_{1;g'g})]W_{g'}, \quad (35)$$

$$\mathbb{S}^{\mathrm{III}}(\tau) = i \sum_{g'} \mathrm{tr}[(\alpha''_{2;gg'})(\alpha_{1;g'g})]W_{g'}. \quad (36)$$

In the above expressions $\mathrm{tr}(A)$ denotes the trace over matrix A, e.g., $\mathrm{tr}(\alpha_{1;g'g}) = \alpha^{xx}_{1;g'g} + \alpha^{yy}_{1;g'g} + \alpha^{zz}_{1;g'g}$. A^{T} stands for the transpose of A. We have used a general function $W_{g'}$ to include the situations with and without the vibronic coupling:

$$W_{g'} = \begin{cases} \exp(-i\omega_{g'g}\tau - \Gamma_{gg'}\tau), & (\text{electronic only}) \\ \exp[-i\omega_{g'g}\tau - g_{g'}(\tau) - \Gamma_{gg'}\tau]. & (\text{vibronic coupled}) \end{cases} \quad (37)$$

Analytical form of the frequency-domain signal exists only when the vibronic coupling is turned off:

$$\bar{\mathbb{S}}(\Omega)\rangle = \begin{pmatrix} \mathbb{S}^{\mathrm{I}}(\Omega) \\ \mathbb{S}^{\mathrm{II}}(\Omega) \\ \mathbb{S}^{\mathrm{III}}(\Omega) \end{pmatrix}^{\mathsf{T}} \begin{pmatrix} 4 - 2\cos^2\theta \\ 3\cos^2\theta - 1 \\ 3\cos^2\theta - 1 \end{pmatrix}, \quad (38)$$

where

$$\mathbb{S}^{\mathrm{I}}(\Omega) = \sum_{g'} \left[\frac{\mathrm{tr}(\alpha''_{2;gg'})\mathrm{tr}(\alpha_{1;g'g})}{\omega_{g'g} - \Omega - i\Gamma_{gg'}} \right], \quad (39)$$

$$\mathbb{S}^{\mathrm{II}}(\Omega) = \sum_{g'} \left[\frac{\mathrm{tr}[(\alpha''_{2;gg'})^{\mathsf{T}}(\alpha_{1;g'g})]}{\omega_{g'g} - \Omega - i\Gamma_{gg'}} \right], \quad (40)$$

$$\mathbb{S}^{\mathrm{III}}(\Omega) = \sum_{g'} \left[\frac{\mathrm{tr}[(\alpha''_{2;gg'})(\alpha_{1;g'g})]}{\omega_{g'g} - \Omega - i\Gamma_{gg'}} \right]. \quad (41)$$

In the case when the vibronic coupling is considered, numerical Fourier transform should be done to $\bar{\mathbb{S}}(\tau)$:

$$\bar{\mathbb{S}}(\Omega) = \int_0^{\infty} \bar{\mathbb{S}}(\tau)e^{i\Omega\tau}. \quad (42)$$

Notes and references

1. Tanaka S, Mukamel S. Phys. Rev. Lett. 2002; 89:043001. [PubMed: 12144479]

2. Schweigert IV, Mukamel S. Phys. Rev. A. 2007; 76:012504.

3. Biggs JD, Zhang Y, Healion D, Mukamel S. J. Chem Phys. 2012; 136:174117. [PubMed: 22583220]

4. Zhang Y, Biggs JD, Healion D, Govind N, Mukamel S. J. Chem Phys. 2012; 137:194306. [PubMed: 23181305]

5. Healion D, Biggs JD, Mukamel S. Phys. Rev. A. 2012; 86:033429.

6. Biggs JD, Zhang Y, Healion D, Mukamel S. J. Chem Phys. 2013; 138:144303.

7. Gel'mukhanov F, Ågen H. Phys. Rep. 1999; 312:87–330.

8. Kotani A, Shin S. Rev. Mod. Phys. 2001; 73:203–246.

9. It is also termed as integrated two-pulse SXRS (I2P-SXRS) or one-dimensional SXRS (1D-SXRS) (e.g., in refs 3,6).

10. McNeil BWJ, Thompson NR. Nat. Photon. 2010; 4:814–821.

11. Beye M, Schreck S, Sorgenfrei F, Trabant C, Pontius N, Schüßler-Langeheine C, Wurth W, Föhlisch A. Nature. 2013; 501:191–194. [PubMed: 23965622]

12. Jolly WL, Hendrickson DN. J. Am. Chem. Soc. 1970; 92:1863–1871.

13. Davis DW, Shirley DA. Chem. Phys. Lett. 1972; 15:185–190.

14. Plashkevych O, Privalov T, Ågren H, Carravetta V, Ruud K. Chem. Phys. 2000; 260:11–28.

15. Hunt WJ, Goddard WA III. Chem. Phys. Lett. 1969; 3:414–418.

16. (a) Ågren H, Carravetta V, Vahtras O, Pettersson LGM. Chem. Phys. Lett. 1994; 222:75–81.(b) Ågren H, Carravetta V, Pettersson LGM, Vahtras O. Physica B. 1995:208–209. 477–480.

17. Stener M, Fronzoni G, de Simone M. Chem. Phys. Lett. 2003; 373:115–123.

18. Lopata K, Kuilen BEV, Khalil M, Govind N. J. Chem. Theory Comput. 2012; 8:3284.

19. Hergenhahn U. J. Phys. B: At. Mol. Opt. Phys. 2004; 37:R89–R135.

20. Minkov I, Gel'Mukhanov F, Friedlein R, Osikowicz W, Suess C, Öhrwall G, Sorensen SL, Braun S, Murdey R, Salaneck WR, Ågren H. J. Chem. Phys. 2004; 121:5733–5739. [PubMed: 15366997]

21. Svensson S. J. Phys. B: At. Mol. Opt. Phys. 2005; 38:S821–S838.

22. Minkov I, Gelmukhanov F, Ågren H, Friedlein R, Suess C, Salaneck WR. J. Phys. Chem. A. 2005; 109:1330–1336. [PubMed: 16833448]

23. Serrano-Andres L, Merchan M, Nebot-Gil I, Roos BO, Fulscher M. J. Am. Chem. Soc. 1993; 115:6184–6197.

24. Palmer MH, Walker IC, Ballard CC, Guest MF. Chem. Phys. 1995; 192:111–125. and Figure 1 therein, with the experimental vacumm UV spectrum of furan, is captured in our Figure 6 for comparison.

25. Christiansen O, Jørgensen P. J. Am. Chem. Soc. 1998; 120:3423–3430.

26. Wan J, Meller J, Hada M, Ehara M, Nakatsuji H. J. Chem. Phys. 2000; 113:7853–7866.

27. Burcl R, Amos RD, Handy NC. Chem. Phys. Lett. 2002; 355:8–18.

28. Rennie EE, Hergenhahn U, Kugeler O, Rüdel A, Marburger S, Bradshaw AM. J. Chem. Phys. 2002; 117:6524–6532.

29. Gromov EV, Trofimov AB, Vitkovskaya NM, Schirmer J, Köppel H. J. Chem. Phys. 2003; 119:737–753.

30. Gromov EV, Trofimov AB, Vitkovskaya NM, Köppel H, Schirmer J, Meyer H-D, Cederbaum LS. J. Chem. Phys. 2004; 121:4585–4598. [PubMed: 15332889]

31. Gromov EV, Lévôque C, Gatti F, Burghardt I, Köppel H. J. Chem. Phys. 2011; 135:164305. [PubMed: 22047237]

32. Ridley T, Lawley KP, Donovan RJ. Phys. Chem. Chem. Phys. 2004; 6:5304–5312.

33. Pastore M, Angeli C, Cimiraglia R. Chem. Phys. Lett. 2006; 426:445–451.

34. Gavrilov N, Salzmann S, Marian CM. Chem. Phys. 2008; 349:269–277.

35. Schreiber M, Silva-Junior MR, Sauer SPA, Thiel W. J. Chem. Phys. 2008; 128:134110. [PubMed: 18397056]

36. Fuji T, Suzuki Y-I, Horio T, Suzuki T, Mitrić R, Werner U, Bonačić-Koutecký V. J. Chem. Phys. 2010; 133:234303. [PubMed: 21186867]

37. Li X, Paldus J. J. Phys. Chem. A. 2010; 114:8591–8600. [PubMed: 20155956]

38. Stenrup M, Larson Å. Chem. Phys. 2011; 379:6–12.

39. Sauri V, Serrano-Andrés L, Shahi ARM, Gagliardi L, Vancoillie S, Pierloot K. J. Chem. Theory Comput. 2011; 7:153–168.

40. Leang SS, Zahariev F, Gordon MS. J. Chem. Phys. 2012; 136:104101. [PubMed: 22423822]

41. Bousquet D, Fukuda R, Maitarad P, Jacquemin D, Ciofini I, Adamo C, Ehara M. J. Chem. Theory Comput. 2013; 9:2368–2379.

42. Zhang Y, Healion D, Biggs JD, Mukamel S. J. Chem. Phys. 2013; 138:144301.

43. Huang K, Rhys A. Proc. R. Soc. Lond. A. 1950; 204:406–423.

44. Pekar SI. J. Exp. Theor. Phys. 1950; 20:510–522.

45. Lax M. 1952; 20:1752–1760.

46. Markham JJ. Rev. Mod. Phys. 1959; 31:956–989.

47. Macak P, Luo Y, Ågren H. Chem. Phys. Lett. 2000; 330:447–456.

48. Ren H, Biggs JD, Mukamel S. J. Raman Spectrosc. 2013; 44:544–559. [PubMed: 23585708]

49. Duschinsky F. Acta Physicochim. URSS. 1937; 7:551–566. and its English translation by C. W. Müler available from http://www.chem.purdue.edu/zwier/pubs/Duschinsky.pdf.

50. Mukamel, S. Principles of nonlinear optical spectroscopy. New York; Oxford: Oxford University Press; 1999. p. 209-259.

51. (a) Becke AD. Phys. Rev. A. 1988; 38:3098–3100. [PubMed: 9900728] (b) Becke AD. J. Chem. Phys. 1993; 98:5648–5652.(c) Lee C, Yang W, Parr RG. Phys. Rev. B. 1988; 37:785–789.

52. Dunning TH. J. Chem. Phys. 1989; 90:1007–1023.

53. (a) Schmidt MW, Baldridge KK, Boatz JA, Elbert ST, Gordon MS, Jensen JH, Koseki S, Matsunaga N, Nguyen KA, Su S, Windus TL, Dupuis M, Montgomery JA Jr. J. Comput. Chem. 1993; 14:1347–1363.(b) Gordon, MS.; Schmidt, MW. Theory and Applications of Computational Chemistry, the first forty years. Dykstra, CE.; Frenking, G.; Kim, KS.; Scuseria, GE., editors. Vol. Chapter 41. Amsterdam: Elsevier; 2005. p. 1167-1189.(c) http://www.msg.chem.iastate.edu/GAMESS/GAMESS.html.

54. Hirata S, Head-Gordon M. Chem. Phys. Lett. 1999; 314:291–299.

55. Valiev M, Bylaska E, Govind N, Kowalski K, Straatsma T, Van Dam H, Wang D, Nieplocha J, Apra E, Windus T, de Jong W. Comput. Phys. Comm. 2010; 181:1477–1489.

56. Szabo, A.; Ostlund, NS. Modern quantum chemistry: introduction to advanced electronic structure theory. Mineola, N.Y.: Dover; 1996.

57. Fronzoni G, Stener M, Decleva P, Wang F, Ziegler T, van Lenthe E, Baerends E. Chem. Phys. Lett. 2005; 416:56–63.

58. Besley NA, Noble A. J. Phys. Chem. C. 2007; 111:3333–3340.

59. DeBeer George S, Petrenko T, Neese F. Inorg. Chim. Acta. 2008; 361:965–972.

60. Besley NA, Peach MJG, Tozer DJ. Phys. Chem. Chem. Phys. 2009; 11:10350–10358. [PubMed: 19890519]

61. Besley N, Asmuruf FA. Phys. Chem. Chem. Phys. 2010; 12:12024–12039. [PubMed: 20714478]

62. Liang W, Fischer SA, Frisch MJ, Li X. J. Chem. Theory Comput. 2011; 7:3540–3547.

63. The symmetry-adapted delocalized molecular orbitals used here does not imply a delocalized core hole. Physically, either the core hole is delocalized within the two equivalent carbons or localized on one atom forms a entangled Bell state and depends on the measurement.[75,76] For simplicity, this work only distinguishes the core excitations from different types C_α or C_β, but not from a particular carbon atom within the same type.

64. Stöhr, J. NEXAFS Spectroscopy. Berlin, Heidelberg, New York: Springer Verlag; 1992.

65. Hua W, Gao B, Li S, Ågren H, Luo Y. Phys. Rev. B. 2010; 82:155433.

66. Duot D, Flament J-P, Giuliani A, Heinesch J, Hubin-Franskin M-J. J. Chem. Phys. 2003; 119:8946–8955. and Figure 5 therein, with the experimental C1s electron energy loss spectroscopy of furan, is captured in our Figure 2 for comparison.

67. Luo Y, Ågren H, Gel'Mukhanov F, Guo J, Skytt P, Wassdahl N, Nordgren J. Phys. Rev. B. 1995; 52:14479–14496.

68. Distefano G, Pignataro S, Innorta G, Fringuelli F, Marino G, Taticchi A. Chem. Phys. Lett. 1973; 22:132–136.

69. Tian, G.; Duan, S.; Hua, W.; Luo, Y. DynaVib, version 1.0. Sweden: Royal Institute of Technology; 2012.

70. Chen X, Tian G, Rinkevicius Z, Vahtras O, Cao Z, Ågren H, Luo Y. Chem. Phys. 2012; 405:40–45.

71. Martin R. J. Chem. Phys. 2003; 118:4775–4777.

72. Here we only retain the terms that appear in the positive-Ω region for the equations derived in ref 5 and rewrite them in a more compact form, with also a few typos corrected.

73. Cartoons are generated by ECCE[77] with logarithm contour isovalue set to −1.5.

74. Allouche A-R. J. Comput. Chem. 2011; 32:174–182. [PubMed: 20607691]

75. Schöffler MS, Titze J, Petridis N, Jahnke T, Cole K, Schmidt LPH, Czasch A, Akoury D, Jagutzki O, Williams JB, Cherepkov NA, Semenov SK, McCurdy CW, Rescigno TN, Cocke CL, Osipov T, Lee S, Prior MH, Belkacem A, Landers AL, Schmidt-Böcking H, Weber T, Dörner R. Science. 2008; 320:920–923. [PubMed: 18487190]

76. Ueda K. Science. 2008; 320:884–885. [PubMed: 18487181]

77. Black, G.; Schuchardt, K.; Gracio, D.; Palmer, B. Computational Science ICCS 2003. Sloot, PMA.; Abramson, D.; Bogdanov, AV.; Gorbachev, YE.; Dongarra, JJ.; Zomaya, AY., editors. Springer Berlin Heidelberg: Lecture Notes in Computer Science 2660; 2003. p. 122-131.

SXRS
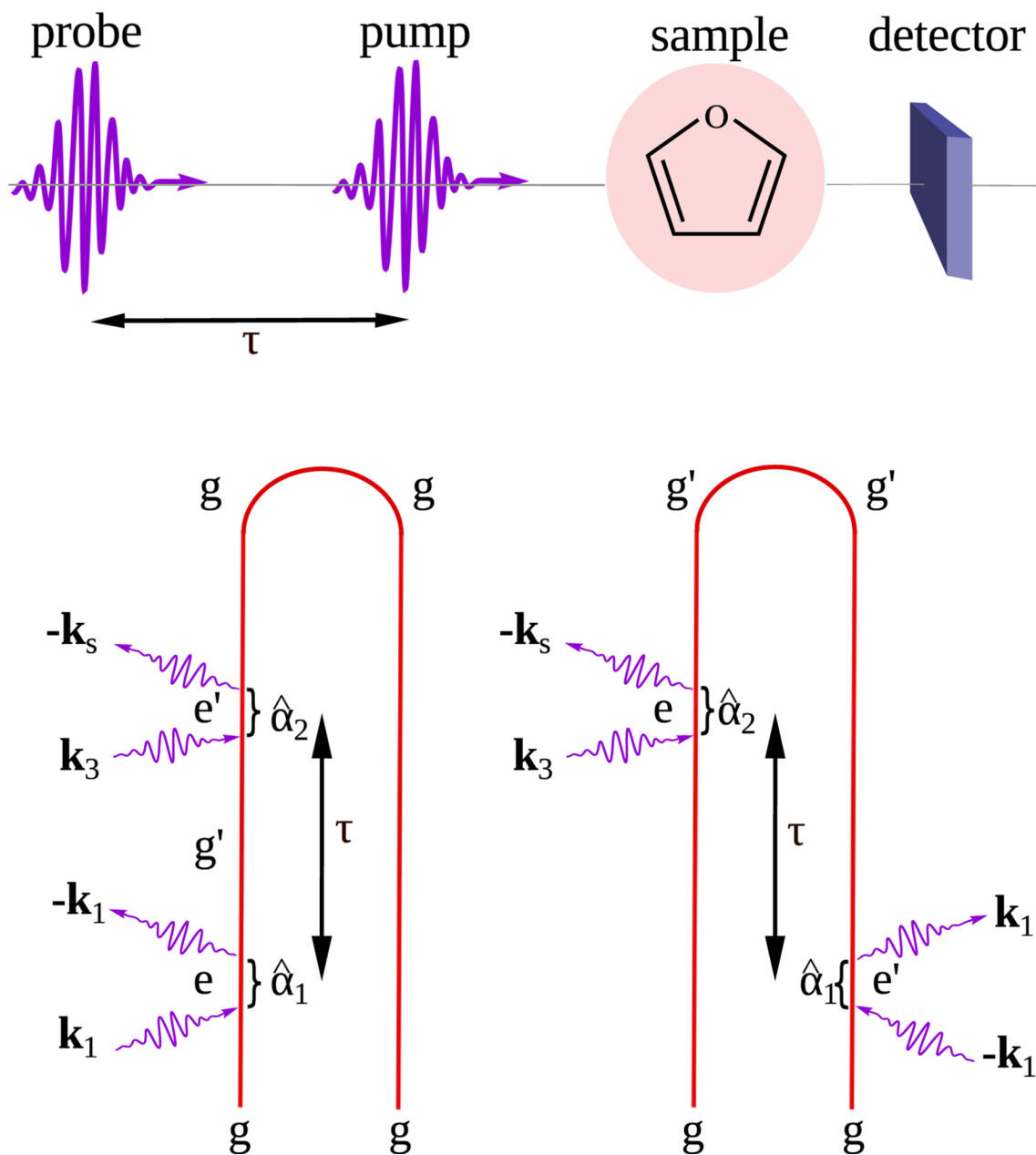
Figure 1.
Attosecond stimulated X-ray Raman spectroscopy: pulse configuration (top) and loop diagrams (bottom). Pulse duration is short compared to pulse delay τ. g, g' and e/e' denote the ground, valence and core excited states, respectively. $\hat{\sigma}_j$ is the effective polarizability operator used to describe the Raman process of pulse j ($j = 1, 2$).
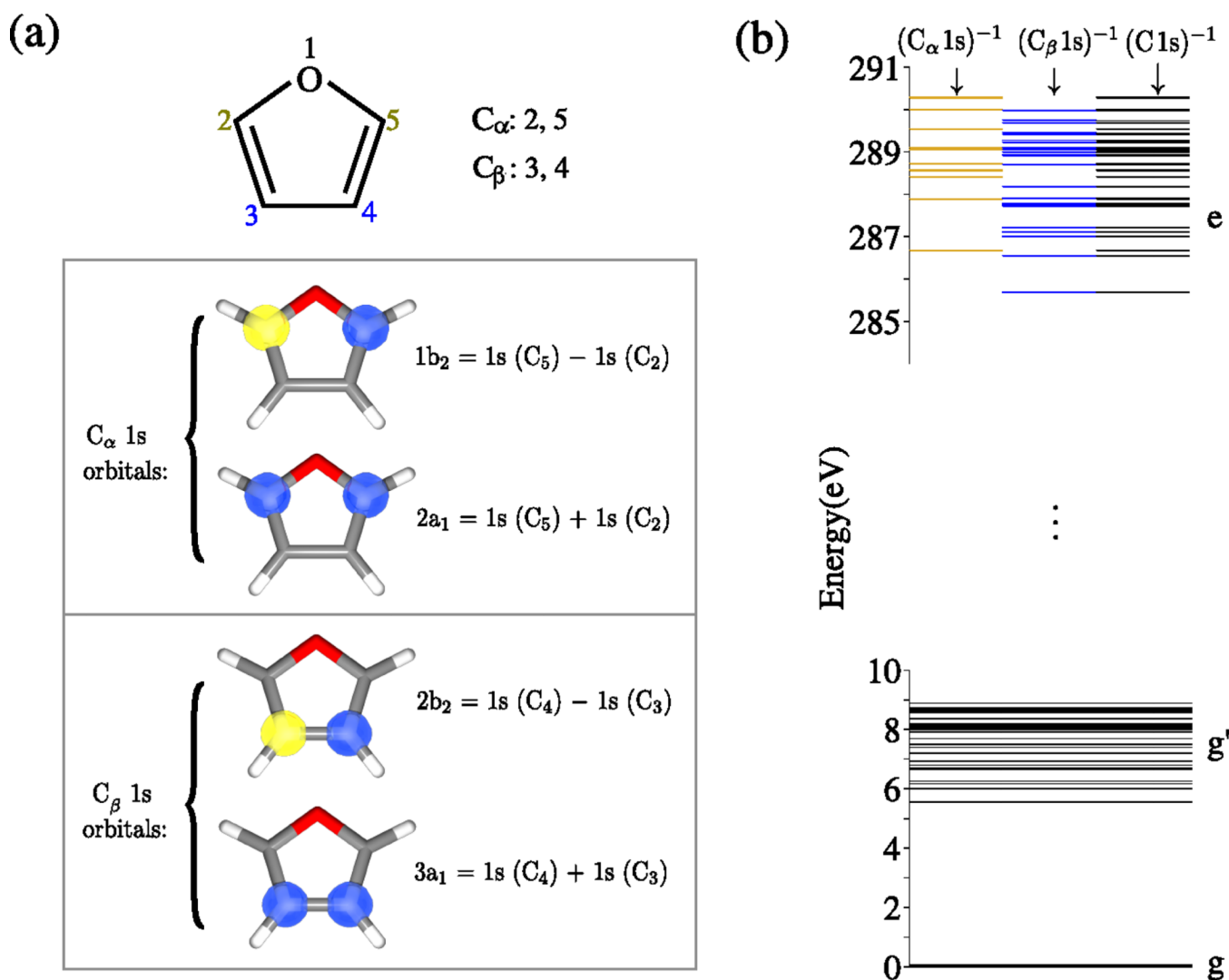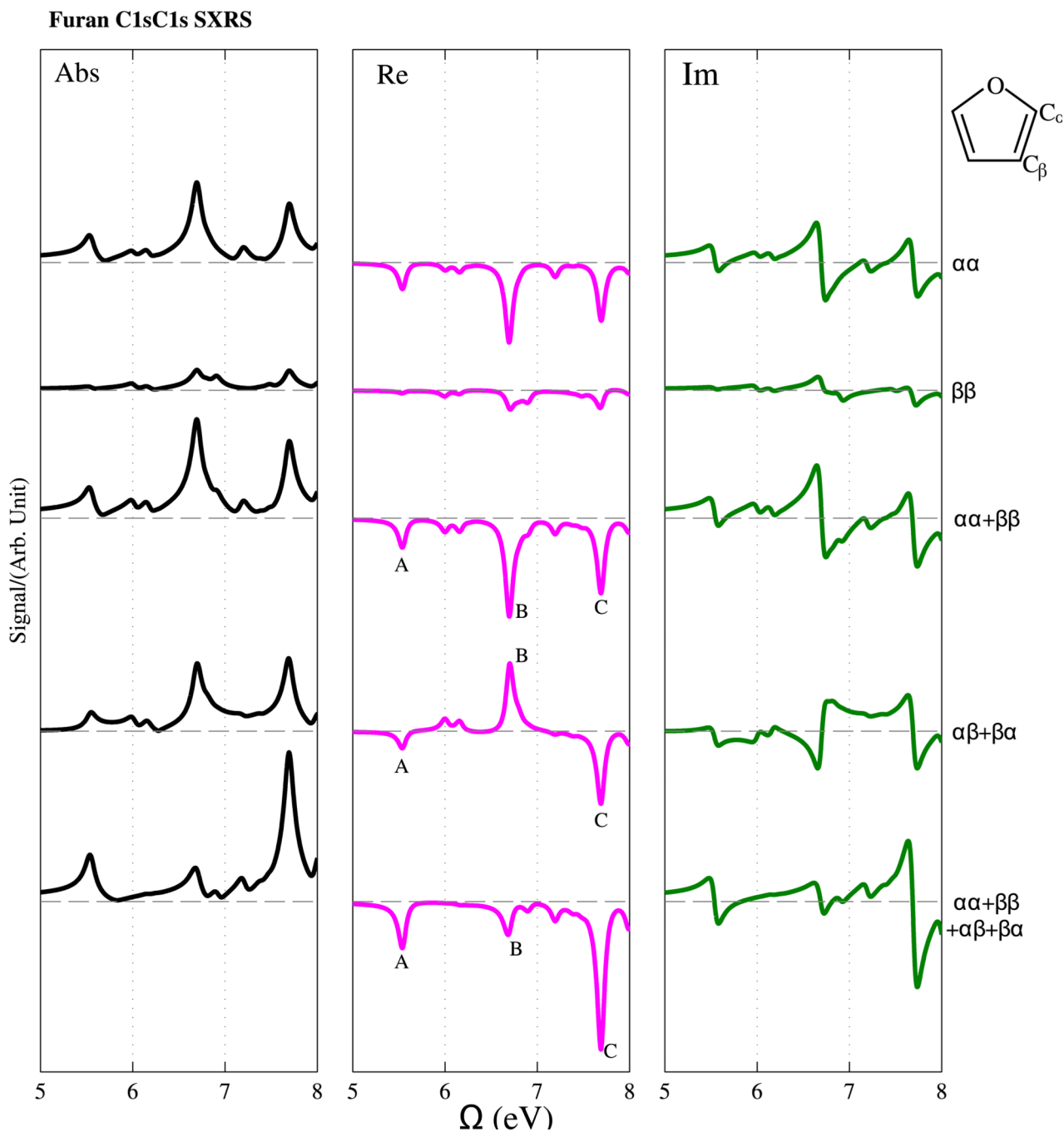
Figure 2.
(a) Structure of furan (top) and the four symmetry-adapted canonical MOs of carbon 1s electrons ($1b_2$, $2a_1$, $2b_2$ and $3a_1$), grouped as C_α 1s and C_β 1s orbitals (bottom).[73] (b) Calculated energy level diagram: valence (g') and C1s core excited (e) states. Three sets of core excited states are shown, where excitations have been restricted from C_α 1s (gold), C_β 1s (blue), and all C 1s orbitals (black). Calculations are performed at TDDFT/TDA B3LYP/aug-cc-pVTZ level and all core levels are uniformly shifted by +10.6 eV to fit experimental XANES.[66]
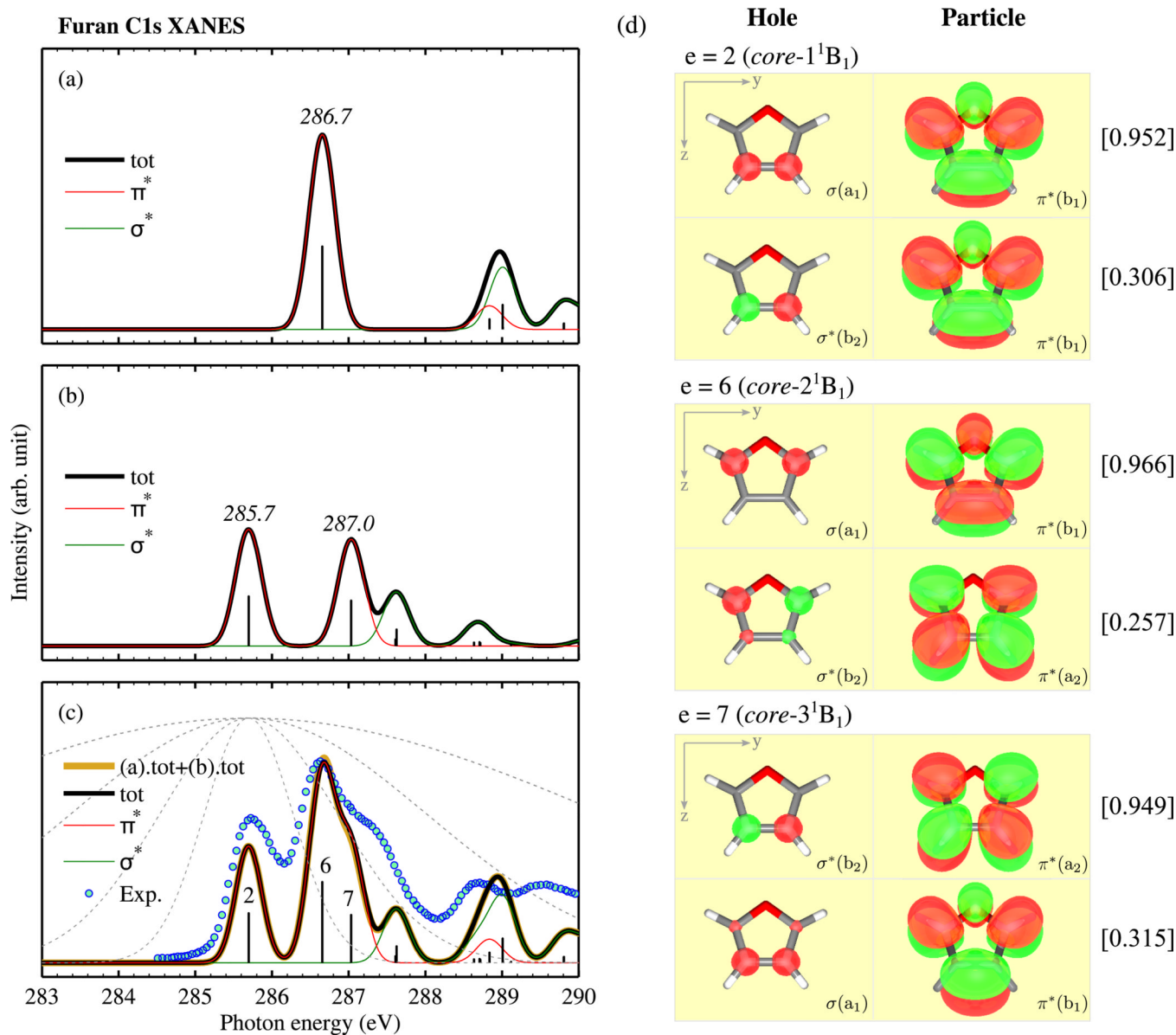
Furan C1s XANES

Figure 3.
Simulated C1s XANES signals of furan obtained by restricting excitations from (a) C_α 1s,
(b) C_β 1s, and (a) all C 1s orbitals. Thick black line: total orientationally averaged spectrum;
red: in-plane 1s $\rightarrow \pi^*$ transitions; green: out-of-plane 1s $\rightarrow \sigma^*$ transitions; vertical lines are
the stick spectra. In panel c, the total spectrum is compared with experiment[66] (blue circles)
and sum of the spectra in panels a and b (gold line). Gray dashes denote the power spectrum
of gaussian pulse used in the C1sC1s SXRS spectroscopy calculations (centered at 285.7
eV), with FWHM bandwidths of 10.96, 5.48, 2.74, 1.37 eV (corresponding to σ_j = 100, 200,
400, 800 as, respectively). (d) Natural transition orbital pairs for major 1s $\rightarrow \pi^{*j}$ transitions
(to core excited states 2, 6 and 7) in panel c.[73] Bonding type and symmetry of each orbital is
given. Occupation numbers are given in brakets.
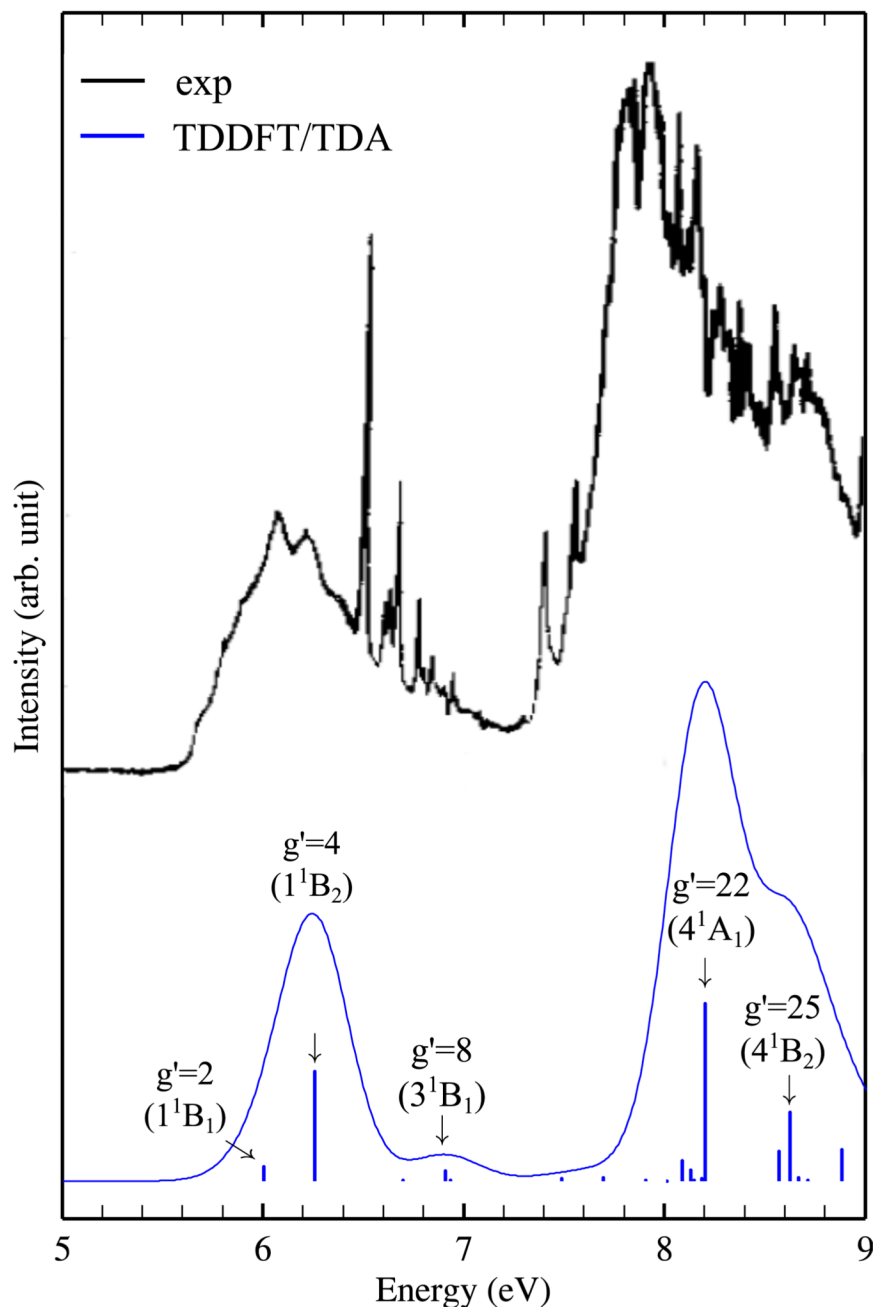
Furan C1sC1s SXRS

Figure 4.
Calculated C1sC1s SXRS signals of furan (absolute, real, and imaginary parts, from left to right panels) from different core-excitation pathways. αα, ββ, αβ, or βα distinguish the two core excitations in furan during the interaction with the pump and probe pulses. αα stands for the pathway that only C_α 1s electrons are excited by the two pulses. Direct addition of the pure signals (αα + ββ) differs from the total signal (αα + ββ + αβ + βα) owing to the significant contribution of the mixed pathways (αβ + βα). The same scale is used in each panel. Major peaks in the middle panel are labeled. Calculations are performed with pulse duration and central carrier frequency set at $\sigma_j = 100$ as and $\omega_j = 285.7$ eV ($j = 1, 2$).
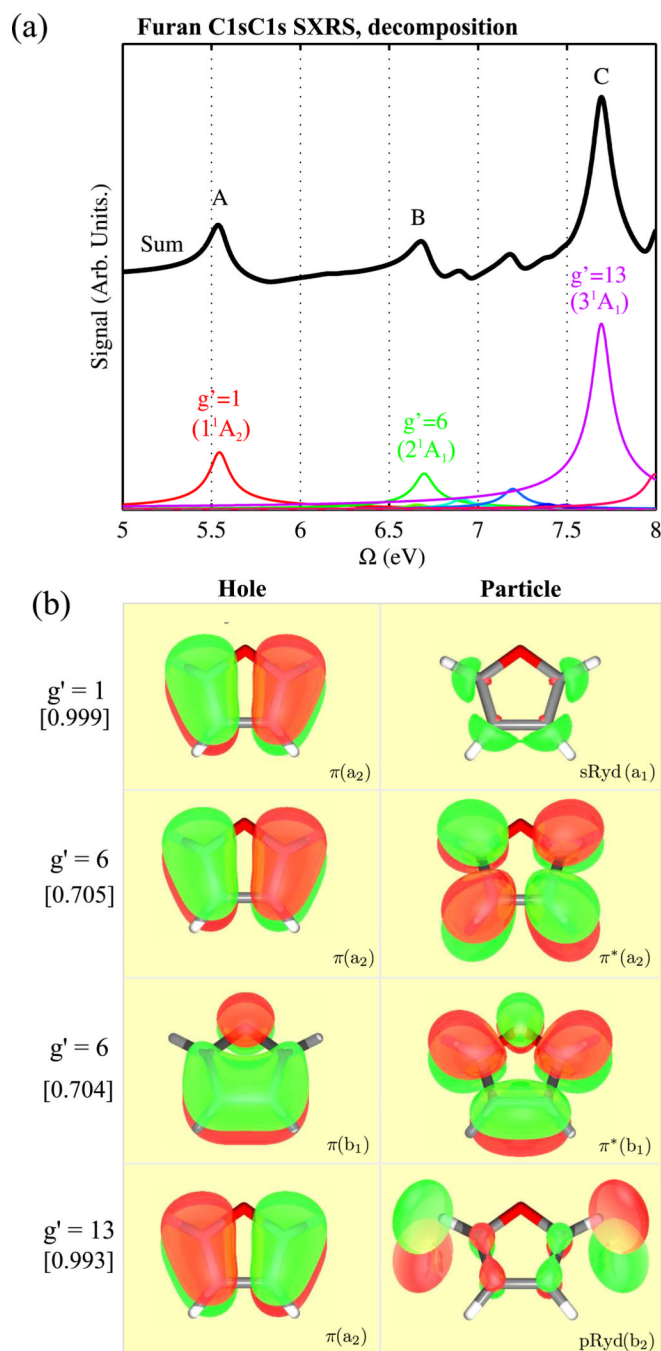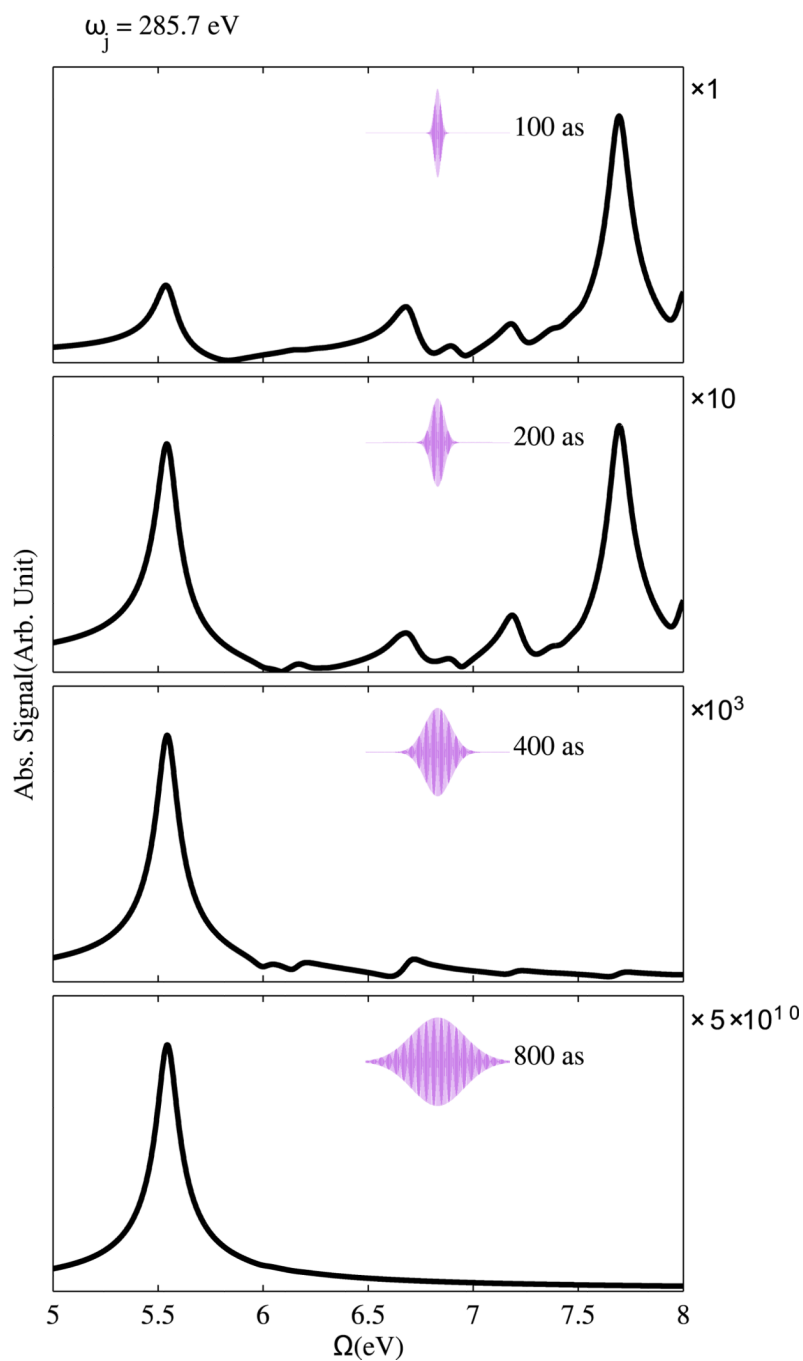
Figure 5.
(a) Calculated total C1sC1s SXRS signals of furan (thick black line) and contributions from different valence excited states (thin colored lines) with dominant states are labeled. (b) Natural transition orbital pairs of major transitions, where hole and particle orbitals appear in the left and right, respectively.[73] Bonding type and symmetry of each orbital is given. Occupation numbers are given in square brakets.

Furan UV absorption

Figure 6.
Simulated UV absorption spectrum of furan in comparison with experiment by Palmer et al.[24] Dominant states are labeled.
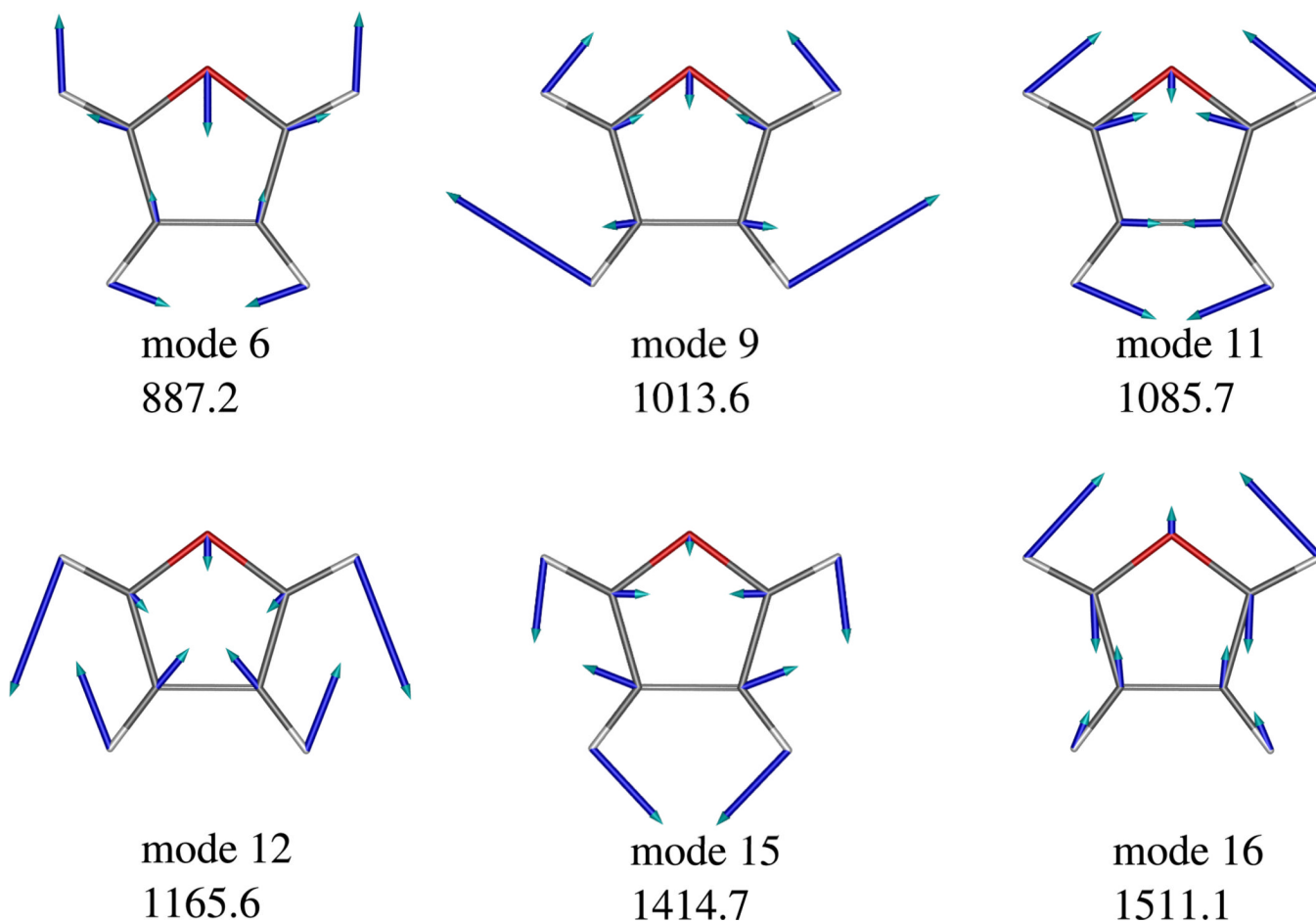
Figure 7.
Dependence of calculated C1sC1s SXRS signal of furan on pulse duration: $\sigma_j = 100, 200, 400$ and 800 as from top to bottom (corresponding to intensity-profile FWHM bandwidth of 10.96 eV, 5.48 eV, 2.74 eV, and 1.37 eV, respectively). The carrier frequency is 285.7 eV.
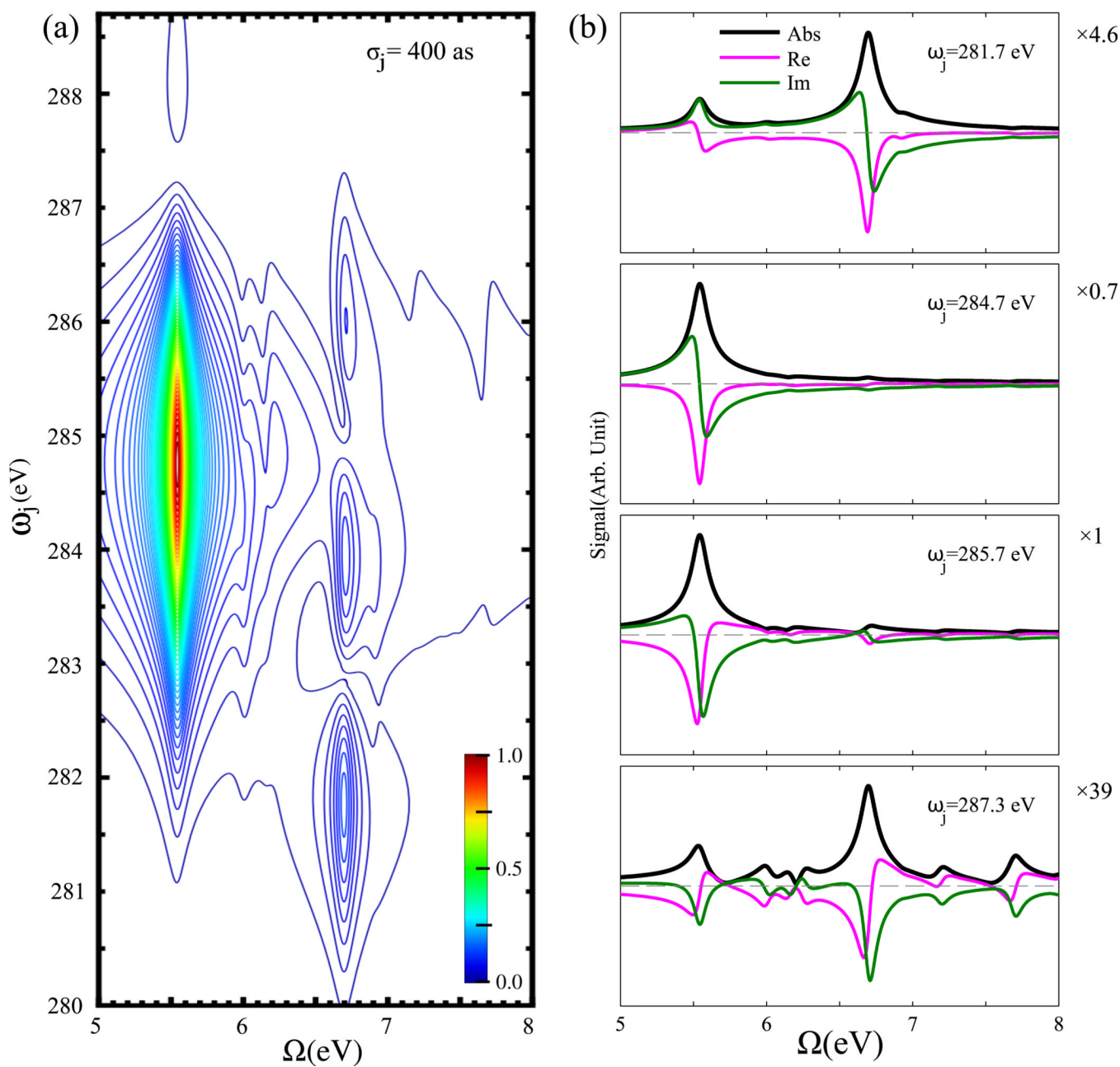
Figure 8.
Dependence of calculated C1sC1s SXRS spectra of furan on the carrier frequency ω_j. (a) Grid plot of absolute signals with respect to ω_j and raman shift Ω. (b) Signals at selected central carrier frequencies: 281.7, 284.7, 285.7 and 287.3 eV (from top to bottom). Pulse durations are $\sigma_j = 400$ as ($j = 1, 2$).

Time domain
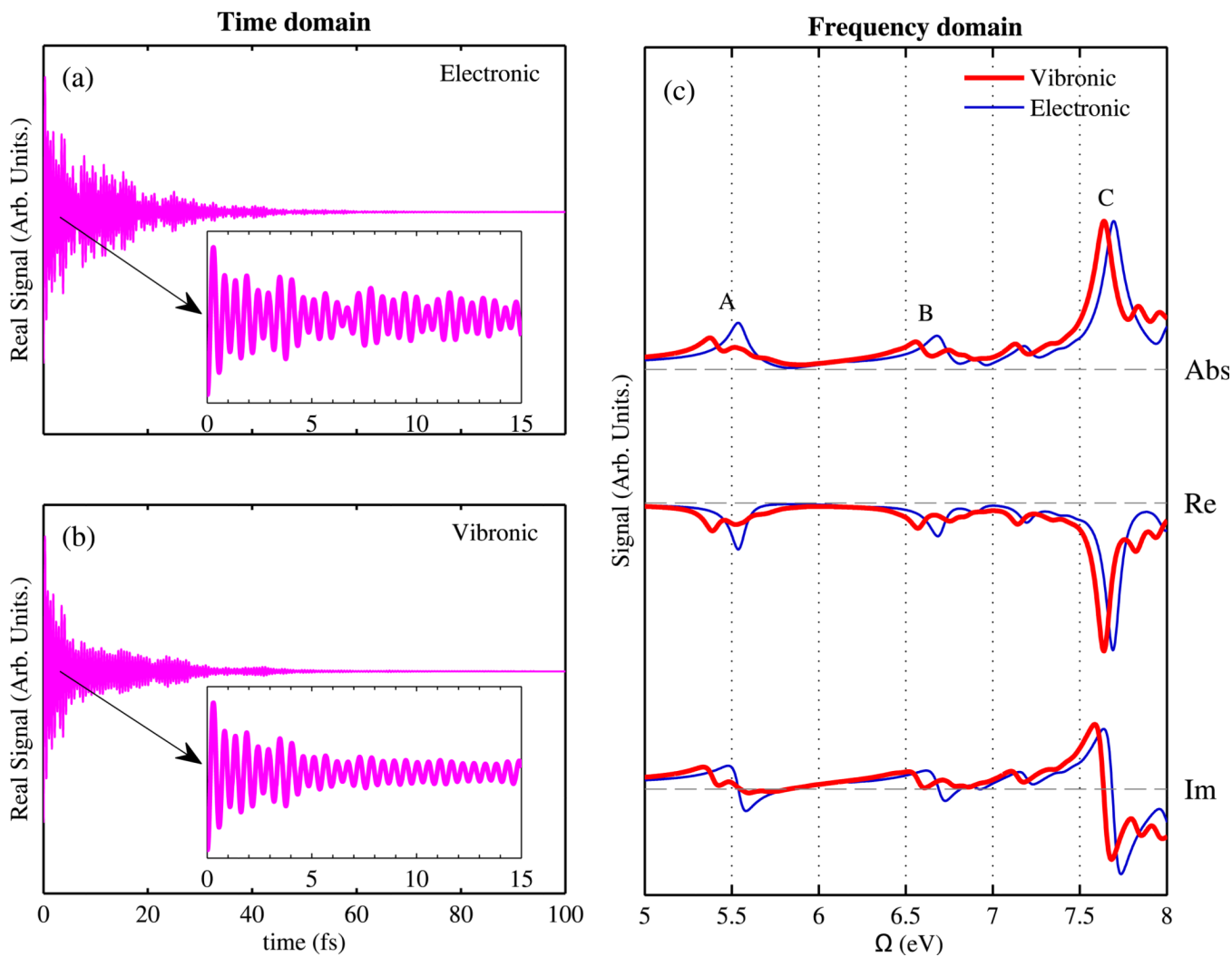
Frequency domain

Figure 9.
Calculated C1sC1s SXRS signals of furan with and without vibronic coupling: (a–b) real part of signals in the time domain; (c) absolute, real and imaginary parts of signals in the frequency domain. In the left panels, the first 15 fs is zoomed out in the inset. Calculations are performed with pulse duration $\sigma_j = 100$ as and central carrier frequency $\omega_j = 285.7$ eV ($j = 1, 2$).

mode 6
887.2

mode 9
1013.6

mode 11
1085.7

mode 12
1165.6

mode 15
1414.7

mode 16
1511.1

Figure 10.
Frank-Condon-active normal modes of furan (see Table 1) with calculated vibrational frequency (in cm^{-1}). These modes correspond to in-plane symmetric vibrations. Cartoons are generated by GABEDIT.[74]

Table 1

Dominant normal modes for selected valence excited states 1, 6, and 13: mode index (k), vibrational frequency (ϖ_k, in cm^{-1}), and vibronic coupling strength $(\lambda_{k,g'} = \sqrt{S_{k,g'}})$. A threshold of $\lambda_{k,g'}$ 0.1 is employed.

k	ϖ_k	$\lambda_{k,g'}$		
		$g'=1$	$g'=6$	$g'=13$
6	887.2	0.45	–	0.16
9	1013.6	0.22	–	–
11	1085.7	0.55	–	–
12	1165.6	0.11	0.33	–
15	1414.7	0.46	0.33	0.22
16	1511.1	0.48	0.66	0.47